Journal of Electromagnetic Analysis and Applications, 2024, 16, 85-101
https://www.scirp.org/journal/jemaa
ISSN Online: 1942-0749
ISSN Print: 1942-0730

Depolarization Degree to Determine Dihedral Attribute of Radar Target

Faisal Aldhubaib

Electronics Department, Faculty of Technological Studies, Public Authority for Applied Education, Shuwaikh, Kuwait
Email: ff.aldhubaib@paaet.edu.kw

How to cite this paper: Aldhubaib, F. (2024) Depolarization Degree to Determine Dihedral Attribute of Radar Target. *Journal of Electromagnetic Analysis and Applications*, **16**, 85-101.
https://doi.org/10.4236/jemaa.2024.166006

Received: November 15, 2023
Accepted: July 26, 2024
Published: July 29, 2024

Abstract

This paper investigates the ability of the depolarization degree, derived from the characteristic polarization states at the resonant frequency set, to identify corner or swept, i.e. dihedral, changes in same-class targets by a metallic wire example. A well-estimated depolarization degree requires a robust extraction of the fundamental target resonance set in two orthogonal sets of fully co-polarized and cross-polarized polarization channels, then finding the null polarization states using the Lagrangian method. Such depolarization degree per resonance mode has the potential to form a robust feature set because it is relatively less sensitive to onset ambiguity, invariant to rotation, and could create a compact, recognizable, and separable distribution in the proposed feature space. The study was limited to two targets with two swept changes of fifteen degrees within normal incidence; under a supervised learning approach, the results showed that the identification rate converging to upper-bound (100%) for a signal-to-noise ratio above 20 dB and lower-bound around (50%) below −10 dB.

Keywords

Polarimetry, Radar Target Recognition, Time-Domain Analysis, Remote Sensing

1. Introduction

In automatic target recognition applications, a radar system operating at the target optic region may use radar signature models, such as range profile [1]-[3], cross-range (imaging) [4]-[6], and micro-Doppler shifts analysis [7] [8]. Nevertheless, this comes at higher complexity and computation costs. On the contrary, a radar system operating at the target fundamental resonance region may apply less complex techniques, such as the complex natural resonance (CNR) signature

[9]-[12], capable of recognizing the radar target class and even the target type when combined with the shape attributes found in the characteristic polarization states (CPSs) [13]-[16].

According to the singularity expansion model (SEM) of a transient response, a series of resonance modes with a set of natural frequencies, damping factor, and residue could resemble the late-time transient portion of a pulsed radar return covering the target fundamental resonance region. The resonant frequency, which is excitation-independent, instills information about the size of the elementary structures; the damping factor is excitation-independent and reflects the material composition. Subsequently, the resonant frequency and damping factor form the first layer in the recognition process to classify or categorize the targets into the same class when the targets have similar dimensions and composition, e.g. mid-sized jetfighters.

In contrast, the residue is excitation-dependent and reflects the mode peak strength, thus used to construct the polarization scattering matrix required to derive the CPS set. Hence, recognizing the target type within the same class requires incorporating shape attributes from the CPS in the decision-making process of the recognition operation [10]. Interestingly, the CPS of a higher fundamental mode has the potential to provide better information about the dihedral or swept degree between joint parts of the target as the electrical interaction between joint target structures increases with a higher resonant frequency.

The CPS set represents the polarization states of reception at which maximum, minimum, or null reception exists in the co-polarized and cross-polarized directions, such that there will be four co-polarized states for a reception: two co-polarized maximums and two co-polarized nulls. Henceforth, evaluated at the target resonant frequency, the co-polarized set of the CPS should be able to unfold the crude degrees of symmetry, depolarization, and tilt in the target substructures along the incidence plane, for targets of similar axes of symmetry, such a symmetry feature becomes redundant for recognition. Meanwhile, the tilt degree associated with a single mode is a variant feature that depends on target rotation in the incidence plane.

On the contrary, the depolarization degree is invariant to the target rotation within the incidence plane and reflects the dihedral degree in corner structures. However, the accuracy or uncertainty in the estimated depolarization set depends on the accuracy of the extracted resonance signature, which usually degrades with ambiguities in the signature modal order and late time onset, plus noise and low resonant to specular return. Therefore, a constraint must apply to how well the estimated resonance signature resembles the original late-time response (quantified by the modal order and variance merit, as explained later) and how this affects the ability of feature samples to form recognizable and separable patterns in the feature space [17]-[20].

Previously, in [12], the author used a feature space of depolarization and tilt

degrees per resonance mode to identify swept changes in a generic aircraft target model within a ten degrees azimuthal sector and achieved a recognition performance of 85% - 100% from −10 to +15 dB. Instead, the present work will attempt to verify the capability of depolarization degree only to identify swept changes of fifteen degrees in a wire target model. The identification method uses a supervised learning approach under noise variations with a weight distance measure metric (depending on the substructure dimension as a fraction of the whole target) to select the most discriminative modes from the target's radar response. The approach could achieve full recognition at a signal-to-noise ratio (SNR) beyond 20 dB for a normal incidence when the specular return and onset ambiguity are at the high end.

The paper's outline is as follows: Sections 2 and 3 outline the mathematical background of the CNR signature, the null polarization states, and the identification algorithm. Section 4 shows the results of the rate of correct (ROC) identification results, and finally, Section 5 reaches conclusions and points out the direction of further studies.

2. Background

2.1. The SEM Signature

Due to a wideband pulse incident covering the fundamental resonance region of the radar target under examination, the SEM theory approximates the transient oscillatory response of the original signal, which begins after some late-time onset, T_L, as a sum of exponentially decaying sinusoids, expressed as $y(t)$:

$$y(t) = \sum_{m=1}^{M} |c_m| e^{-\delta_m t} \cdot \sin\left(\omega_m t + \arg(c_m)\right) \tag{1}$$

The parameter M defines the modal order of the signature (by default, set it equal to the number of cardinal target substructures); c_m defines the complex residues; δ_m defines the damping factor; ω_m defines the angular resonant frequencies. Notably, the residue and damping factors are essential parameters used to estimate the energy of the resonance. As a rule of thumb, the late-time onset commences after the incident wave transits the farthest tip of the target along the incident plane. The farthest tip appears as the farthest pulse peak in the return response and before the commencement of the oscillatory return (see Equation (2) in [12]). Another way is to take the reciprocal of the first fundamental frequency (if well excited) and add the pulse width duration.

The matrix pencil of function (MPOF) algorithm may be used to extract and estimate the three resonance parameters in two steps: first, the solution of an ill-conditioned matrix of $y(t)$ formed by delays of $y(t)$ and then find the roots of a polynomial by the singular value decomposition (SVD) [21].

The variance amplitude figure (VAF) metric quantifies the degree of uncertainty in the estimated resonance set by measuring the similarity of the approximated signal, $y(t)$, to the original signal, $x\ (t > T_L)$, after the selected onset, T_L [22].

$$\mathrm{VAF} = 100 * \left(1 - \frac{\mathrm{var}(x) - \mathrm{var}(y)}{\mathrm{var}(x)}\right) \tag{2}$$

The "var" defines the variance.

Henceforth, the signature signal *y(t)* must fulfill two constraints to derive a reliable CPS set: have consistent *M* and sufficient VAF merit in all polarization channels.

2.2. The Characteristic Polarization States (CPSs)

For quad-polarization directions, the backscattered responses in orthogonal linear basis (*h, v*) of transmission and reception directions form a real-time dependent matrix $\boldsymbol{S}^{2\times 2}$ as follows:

$$\boldsymbol{S} = \begin{bmatrix} y_{hh}(t) & y_{hv}(t) \\ y_{vh}(t) & y_{vv}(t) \end{bmatrix} \tag{3}$$

The subscripts *hh* and *vv* denote the co-polarized scattering directions or channels, while *hv* and *vh* denote the cross-polarized scattering channels (reciprocal for monostatic case). Since the resonance residue is the only polarization-dependent term, a reside polarization scattering matrix (RPSM), namely $\boldsymbol{C}^{2\times 2}$, can thus describe the target polarization scattering at a *single* resonance by dropping the time dependence term, i.e. $\mathrm{e}^{-(\delta_m + j\omega_m)t}$, as follows:

$$\boldsymbol{C} = \begin{bmatrix} c_{xx} & c_{yx} \\ c_{xy} & c_{yy} \end{bmatrix} \tag{4}$$

Therefore, constructing the RPSM requires that the associated residue of this resonance be extractable from the temporal response by the MPOF in all polarization channels.

On reception, the signal is split into co- and cross-polarized channels, with the power at the antenna terminals established separately for each channel. The complex residues, c_{hh}, and c_{vv}, denote the co-polarized scattering coefficients, with c_{yx} and c_{xy} denoting the cross-polarized scattering coefficients, and are equal for the reciprocal (monostatic) case. The constraint of having consistent modal order in the matrix means that the co- and cross-polarized terms must have the same modal order, i.e. $M_{hh} = M_{yx} = M_{xy} = M_{vv}$ for every extraction trial.

Next, the related power in the co-polarized channels is a function of the antenna polarization state, represented by Stokes vector $\boldsymbol{g}$, as follows:

$$P(g_1, g_2, g_3) = \frac{1}{2}\boldsymbol{g} \cdot \mathrm{diag}(1,1,1,-1) \cdot \left(\boldsymbol{R} \cdot \left([\boldsymbol{C}] \mathrm{U} [\boldsymbol{C}]^*\right) \cdot \boldsymbol{R}^{-1}\right) \cdot \boldsymbol{g}^{\mathrm{T}} \tag{5}$$

where $\boldsymbol{R} = \begin{pmatrix} 1 & 0 & 0 & 1 \\ 1 & 0 & 0 & -1 \\ 0 & 1 & 1 & 0 \\ 0 & j & -j & 0 \end{pmatrix}$, the Stokes vector $\boldsymbol{g} = [g_0, g_1, g_2, g_3]$ defines the antenna's polarization state in terms of g_0 as total, g_1 as linear *h*-*v*, g_2 as linear at ±45˚, and g_3 as circular power portions, respectively. The product ($[\boldsymbol{C}] \otimes [\boldsymbol{C}]^*$)

defines the Kronecker product of matrix $\boldsymbol{C}$ and its conjugate. Applying the Lagrangian multiplier method to the power function in (5) subject to the constraint function ($\Phi(g_1, g_2, g_3) = \sqrt{g_1^2 + g_2^2 + g_3^2} - g_0$) to optimize the received power yield the following three simultaneous equations:

$$\frac{\partial P}{\partial g_n} - \mu \frac{\partial \Phi}{\partial g_n} = 0, \quad n = 1, 2, 3. \tag{6}$$

where, μ is the Lagrangian multiplier, which optimizes the power quantity rate of change as a function of the constraint variables. Solving (6) produces two pairs of co-polarized CPS, the orthogonal co-pol max pair ($cm_{1,2}$)and the co-pol null pair ($cn_{1,2}$), which engulf the copol max of minor power, forming a polarization fork around a great circle, as depicted in Figure 1. The variableg_3 of the major co-pol max reflects the symmetry (0 for the symmetrical target, ±1 for the nonsymmetrical target). The co-pol null pair set is not orthogonal but defines a characteristic anglerelated to the depolarization degree, γ, as follows:

$$\gamma = \frac{\mathrm{dot}(\boldsymbol{g}_{cn1}, \boldsymbol{g}_{cn2})}{\|\boldsymbol{g}_{cn1}\| \|\boldsymbol{g}_{cn2}\|} \tag{7}$$

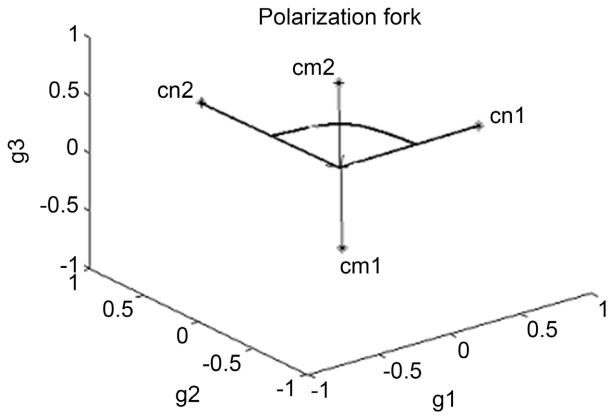

Figure 1. Characteristic polarization state pairs form a polarization signature (polarization fork).

3. The Method

The following steps summarize and illustrate the procedures:

1) Derive the transient response of the co- and cross-polarized directions {*hh*, *yx*; *xy*, *vv*} where $x \perp y$ (see Figure 5, for example).

2) Measure the uncertainty in the resonance extraction (see Figure 6, for example).

3) Use an ensemble average approach to the constraints on the modal order and the VAF merit (see Figure 7, for example).

4) Extract the resonance residue using the MPOF method (see Table 2, for example).

5) Find the co-pol null states of each resonance and then the depolarization degree per resonance (see Table 3 and Table 4, for example).

6) Determine the weighted feature set for all known targets (two in this case) (see Figure 8, for example).

7) Use a supervised learning approach to calculate the rate of correct identification vs. *SNR* (see Figure 9, for example).

3.1. The Feature Set

Assuming that the targets have identical substructures and dimensions, as in the case of same-class aircraft targets, the problem is to discriminate or identify these same-class targets by their dihedral shape feature per resonance mode. Therefore, it is desirable to quantify the shape variant degree ($\Delta\lambda$) of a substructure (X), e.g. wings, for ith target, say q_i, compared to a reference target, q_{ref}, as follows:

$$\Delta\lambda_X\left(q_i\right)=\frac{\lambda_X}{\Omega_\lambda}\frac{\left|\theta_i-\theta_{ref}\right|}{\Omega_\theta} \tag{8}$$

where the angle θ denotes the substructure swept angle about the main body direction ranges from parallel, that is, zero, to perpendicular, i.e. max degree Ω_θ (=90˚); the term λ_X denotes the dimension of the substructure of interest; the term Ω_λ denotes the total sum of substructure dimensions of interest.

Then, for the number of training targets (Q) with prior probabilities of $P(q_i)$, $i=1,\cdots,Q$, express the average shape variant ($\Delta\lambda_X$) of a substructure X as follows:

$$\Delta\lambda_X=\frac{1}{Q-1}\sum_{n=1}^{Q}P\left(q_n\right)\cdot\Delta\lambda_X\left(q_n\right)\Delta \tag{9}$$

For multiple substructures $X_1,\cdots,X_{M'}$ that are excited by M resonances, then the weighting of the depolarization degree, γ, per mth resonance by the averages ($\Delta\lambda_{X1,\cdots,M'}$) forms the proposed feature set $\boldsymbol{F}$ in M-dimensional space as follows:

$$\boldsymbol{F}=\left[\Delta\lambda_{X_1}\cdot\gamma_1,\cdots,\Delta\lambda_{X_M}\cdot\gamma_M\right] \tag{10}$$

To make the feature set as compact as possible, and hence, fewer distance computations and more separable feature patterns of different targets, select the 1,…., M^* resonances with ($\Delta\lambda_X$) above a certain upper threshold or discard the ones below a certain lower threshold.

3.2. The Learning Approach

In the training stage, the algorithm begins by estimating the expected (mean) feature set, namely the training prototype, by generating, per resonance, a sample distribution of the feature set with noise perturbation per target. Then, in the testing stage, the algorithm assigns the test sample corrupted by noise from a target under test to the stored target database with the minimum distance aggregated across the M' resonances of interest. The following steps summarize the identification approach for trained targets (Q_{tr}) and test targets (Q_{ts}) as follows:

1) Training stage: For N realizations or trials, generate the noisy sample distribution of the set as $\boldsymbol{F}_i = \boldsymbol{F}_{0,i}; \cdots; \boldsymbol{F}_{N-1,i}$, then the training prototype ($\tilde{\boldsymbol{F}}$) is the expected value, i.e. the first moment, expressed as follows:

$$\tilde{\boldsymbol{F}} = \frac{1}{N-1}\sum_{n=0}^{N-1}\boldsymbol{F}_n \tag{11}$$

2) Test stage: Taking one of the stored targets as the test target q_j, where its feature set samples are considered the test sample set ($\boldsymbol{F}_j$), then across M' modes of interest, measure the aggregate distance (D) between the nth test sample ($\boldsymbol{F}_{n,j}$) from target q_j and the training prototype $\tilde{\boldsymbol{F}}_i$ of the ith target q_i by a distance metric ||.|| as follows:

$$D_{n,M'}(i,j) = \frac{1}{M'-1}\sum_{m=1}^{M'}\left\|\tilde{\boldsymbol{F}}_i(m) - \boldsymbol{F}_{n,j}(m)\right\| \tag{12}$$

3) Repeating the previous step for $i = 1, \cdots, Q_{tr}$ cataloged targets will generate ($N.Q_{tr}$) distances, i.e. $D_{n,M'}(i,j)$, $n = 0, \cdots, N-1$ and $i = 1, \cdots, Q_{tr}$, for a single test target q_j.

4) Assign sample $\boldsymbol{F}_{n,j}$ to ith target q_i if the minimum distance $D_{n,M}(i,j)_{\min} > D_{n,M}(\neq i,j)_{\min}$ + distance threshold (h), or else declare unable to assign and discard this result if $D_{n,M}(i,j)_{\min} \le D_{n,M}(\neq i,j)_{\min} + h$. The user selects the threshold, h, as a fraction of the maximum distance $D_{\max} = \sqrt{r_1 + \cdots + r_{M'}}$ where $r = \max(\gamma)$, i.e. $r = 1$.

5) If the jth and ith targets of the minimum distance are the same, i.e. $D_{n,M'}(i, j = i) = D_{\min}$ then declares able to assign to the correct target (correct decision), incrementing the number of correct target identification (A_j) for the jth target, else declare unable to assign to the correct target (incorrect decision).

6) Repeat the previous step for each test target; then, the ROC is the ratio of the total number of correct target identifications (A) to the product (Q_{ts}. Q_{tr}. N), expressed as a percentage.

$$\mathrm{ROC} = \frac{A_1 + \cdots + A_{Q_{tr}}}{Q_{ts} \times Q_{tr} \times N} \times 100 \tag{13}$$

7) Repeat previous steps with different $SNRs$ to establish the curve of the ROC vs. SNR levels. For Q_{ts} targets with the same prior probability, the lower bound of the ROC curve, at least theoretically, will set approximately around $100/Q_{ts}$, e.g. 50% for $Q = 2$, %33 for $Q = 3$.

Henceforth, the results will show how well the identification algorithm performs under modal order and VAF constraints, with shape variant weighting the feature set per resonance mode.

4. Simulation and Results

The EM software FEKO [23] enables the modelling of a wire target. It calculates the frequency response by the method of moments, setting the maximum frequency preferably at twice the highest resonant frequency of interest. A wire target model is sufficient for our purpose, as the dihedral structures provide sufficient

polarization information to implement the identification algorithm. Figure 2 depicts the configuration of the target dimensions and shape. The angle θ_w defines the wing's swept angle, whereas θ_t defines the tail's swept angle with the longitudinal axis.

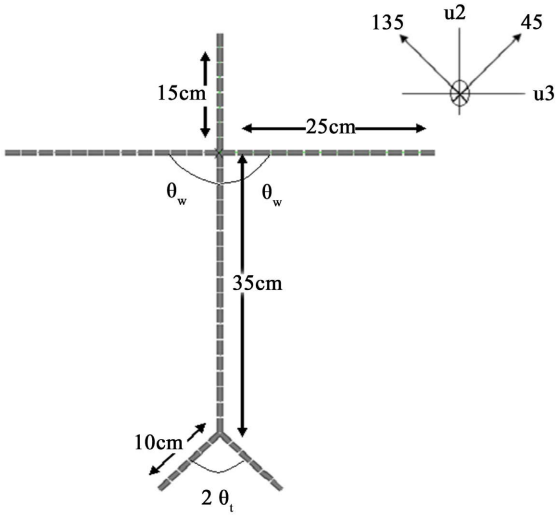

Figure 2. The aircraft wire model configuration with normal incidence looks in the u_1 direction. The angles θ_w, and θ_t give the model different shapes but do not change the dimensions.

The simulation (with values depicted in Table 1) uses two different swept sets $(\theta_w, \theta_t) = (30^\circ, 60^\circ)$ and $(45^\circ, 45^\circ)$ to have two models with a swept difference of 15° to validate the feature set robustness. Having more than two test targets will only decrease the lower bound of the ROC curve, but the approach is still valid for two targets. Changing the angles θ_w and θ_t does not affect the geometrical dimensions (i.e. a similar set of resonant frequencies) but leads to different shapes and, subsequently, different polarization characteristics.

Table 1. Feko simulation values.

Parameter	Value
Start frequency	1.9 MHz
Stop frequency	1 GHz
Number of frequency points	512
Excitation source voltage	1V
Incidence direction	Normal
Wire radius	0.33 cm
Number of segments	83
SEM modal order	4
Late-time onset	25 ns

This configuration led to four dominant resonances, i.e. $M = 4$, corresponding to the mid, the nose-wings, the wings-mid, and the tails, respectively, as depicted in Figure 3. However, only the second to fourth-order resonances reflect the dihedral features of the target.

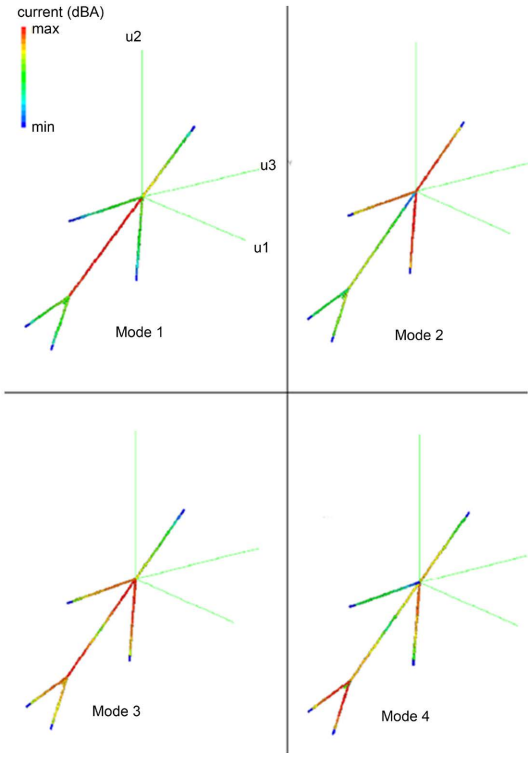

Figure 3. The current distribution per mode shows the excited section of the aircraft model.

In Figure 4, the current distributions of four selected segments belonging to (the nose, wing, mid, and tail) sections of the model demonstrate that the resonances, i.e. reflected by peaks in the response, correspond mainly to sections of the mid, the wings, the nose, and the tails, respectively. The jointed nose, mid, and skewed wing effect will be more profound on the total response, as seen in Figure 4. Each section has a different resonant frequency depending on its dimensions, but both models have the same resonant frequency set overall. Therefore, both models are assumed to be electrically similar. Figure 5 shows the temporal response for both models after Fourier Transforming the frequency response. In general, the x-pol returns of both models display less specular reflections and better oscillatory returns (more robust modes). Henceforth, with different noise levels, anticipate that some resonance residue may be difficult to attain in all quadrature polarization channels.

Figure 6 presents two trials of MPOF extraction against *SNR* from 0 to +40 dB, leading to the frequency distribution of four resonances with noise. Both models' resonance sets are generally closely identical, as expected, especially the first and second sets. This trial evaluation displays modes around 180, 290, 375 - 410, and 650 MHz. In addition, there are slight and uncorrelated shifts in the

frequency of the extracted modes from channel to channel and from model to model. Shifts in the third and fourth sets are more noticeable, suggesting that allowing a guard or margin band when grouping residues from the quadrature polarization channels is good practice. The fourth-ordered resonance caused the most uncertainty in the signature modal as it was very susceptible to noise below 20dB, suggesting either reducing the modal order with lower SNR or using ensemble averaging to enhance the SNR.

To satisfy a well-estimated resonance signature with noise perturbation, i.e. an approximated signal of consistent modal order and high VAF, take the ensemble average of the original signal before MPOF extraction. As shown in **Figure 7**, applying the ensemble average against noise can guarantee consistency in the modal order M and improve the VAF, e.g. by four folds at 0 dB from 20% to 80%.

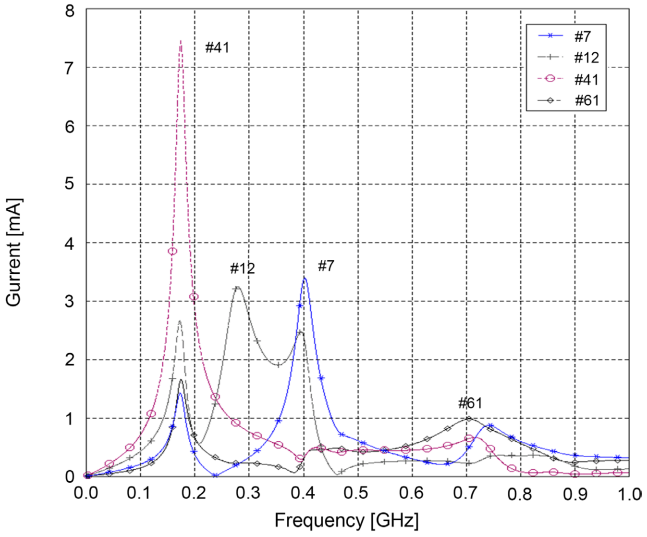

(a) Model A

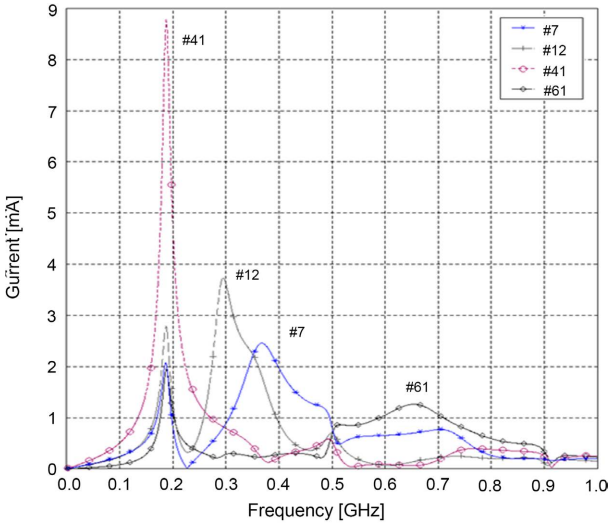

(b) Model B

Figure 4. The current-frequency responses in hh-pol of the selected segments belonging to the nose (#7), wing(#12), mid(#41), and tail stabilizer (#61), respectively.

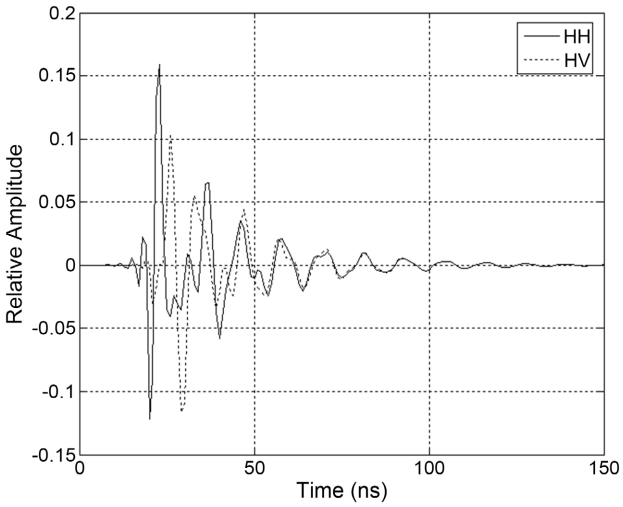

(a) Model A

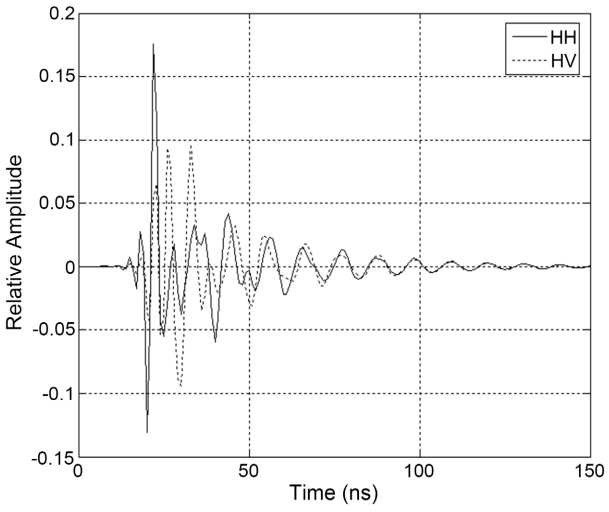

(b) Model B

Figure 5. Calculated temporal responses of both models in HH and HV channels.

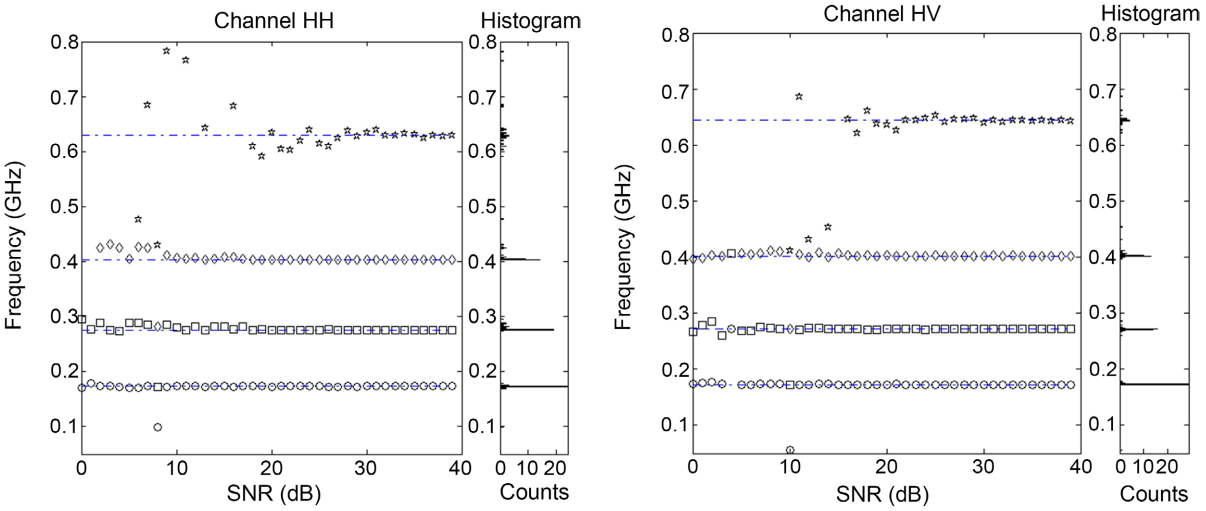

(a) Model A

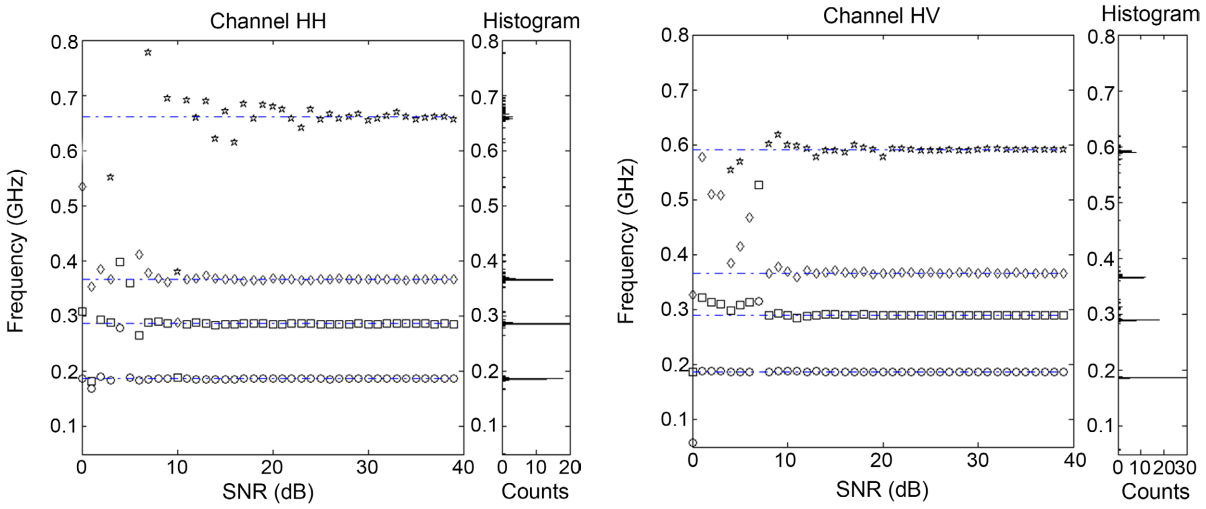

(b) Model B

Figure 6. The fourth-order resonant frequency distributions in (hh and hv) channels against *SNR* for (a) Model A and (b) Model B. There are three distinctive resonances in the ranges 144 - 155, 270 - 300, and 450 - 500 MHz. Generally, higher modes are more susceptible to noise, e.g. the fourth mode below 20 dB.

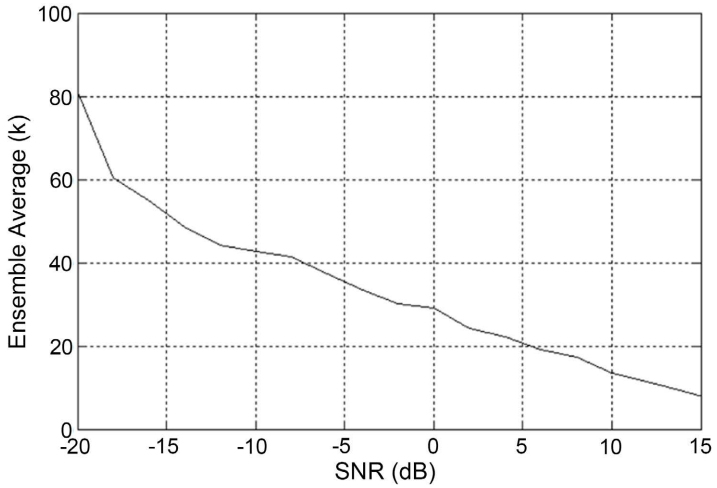

Figure 7. Ensemble average per SNR for $M = 4$ and VAF > 80%.

After applying the MPOF to the temporal backscattered signal of Model A, a set of four resonances exist with complex residues as shown in **Table 2**, inserting the complex residues into (4) for each mode and then applying (5) and solving the co-pol CPS set at each resonance mode, as listed in **Table 3** and **Table 4**, illustrating that the target models have a different CPS set at each resonance and, subsequently, different physical attributes. For the first model, at the first resonance, the geometry is forecasted to be highly long as the dot product $g_{cn1} \cdot g_{cn2} = 1$ and tilted about 45˚ (as $1/2\tan^{-1}(g_2/g_1) = 45^\circ$ for $[g_{cn1} + g_{cn2}]$); thus corresponding mainly to the midsection. The second to the fourth have similar CPS sets with the non-linear property as $g_{cn1} \cdot g_{cn2} \neq 1$, forecasting a dihedral structure. These attributes of the CPS at the dominant resonances agree with what a priori known about the target composite is. In particular, the g_3 of the co-pol max set, $cm_{1,2}$,

for all resonances is zero, indicating that all target geometries are symmetrical.

Table 2. The scattering coefficients of Model A.

Resonance order	c_{hh}	c_{yx}	c_{vv}
1	0.49 − 0.13j	0.37 − 0.38j	−0.49 + 0.13j
2	0.92 + 0.73j	0.28 + 0.11j	−0.92 − 0.73j
3	−1.44 + 3.64j	0.64 + 0.03j	1.44 − 3.64j
4	−0.97 − 2.23j	-0.65 + 0.15j	−0.97 − 2.23j

Table 3. The CPS of Model A.

Mode order	CPS	g_1	g_2	g_3	P_c
1	cm_1	0	1	0	1
	cm_2	0	−1	0	0
	cn_1	**0**	**−1**	**0**	**0**
	cn_2	**0**	**−1**	**0**	**0**
2	cm_1	0	1	0	1
	cm_2	0	−1	0	0.34
	cn_1	**0**	**−0.26**	**0.97**	**0**
	cn_2	**0**	**−0.26**	**−0.97**	**0**
3	cm_1	0	1	0	1.0
	cm_2	0	−1	0	0.51
	cn_1	**0**	**−0.16**	**0.98**	**0**
	cn_2	**0**	**−0.16**	**−0.98**	**0**
4	cm_1	0	1	0	1
	cm_2	0	−1.0	0.0	0.32
	cn_1	**0**	**−0.27**	**0.96**	**0.0**
	cn_2	**0**	**−0.27**	**−0.96**	**0.0**

Table 4. Compared to the first model, the CPS results of Model B.

Mode order	CPS	g_1	g_2	g_3	P
1	cm_1	0.0	1.0	0.0	1.0
	cm_2	0.0	−1.0	0.0	0.0
	cn_1	**0.0**	**−1.0**	**0.0**	**0.0**
	cn_2	**0.0**	**−1.0**	**0.0**	**0.0**

Continued

2	cm_1	0.0	1.0	0.0	1.0
	cm_2	0.0	−1.0	0.0	0.03
	cn_1	**0.0**	**−0.72**	**0.7**	**0.00**
	cn_2	**0.0**	**−0.72**	**−0.7**	**0.00**
3	cm_1	0.0	1.0	0.0	1.0
	cm_2	0.0	−1.0	0.0	0.71
	cn_1	**0.0**	**−0.08**	**1.0**	**0.0**
	cn_2	**0.0**	**−0.08**	**−1.0**	**0.0**
4	cm_1	0.0	1.0	0.0	1.0
	cm_2	0.0	−1.0	0.0	0.0
	cn_1	**0.0**	**−0.87**	**0.49**	**0.0**
	cn_2	**0.0**	**−0.87**	**−0.49**	**0.0**

Next, to demonstrate the ability of the co-null state to discriminate between similar type models, the feature space per resonance mode consists of samples or realization of the dihedral degree generated at this mode with a predetermined SNR. Table 3 derives and lists the CPS set at each resonance for Model A.

Comparing the results of both tables for Models A and B, their co-null set at the second to fourth resonance demonstrates the significant difference, complying with the swept angle change made to the wings and tails.

Figure 8 depicts the distribution of the third and fourth modes at 20dB *SNR*, showing normal distributions that are separable with high VAF. These samples will form the test prototypes in the 20 dB testing stage later, whereas the expected prototype constitutes the 20 dB training prototype stored in the cataloged database.

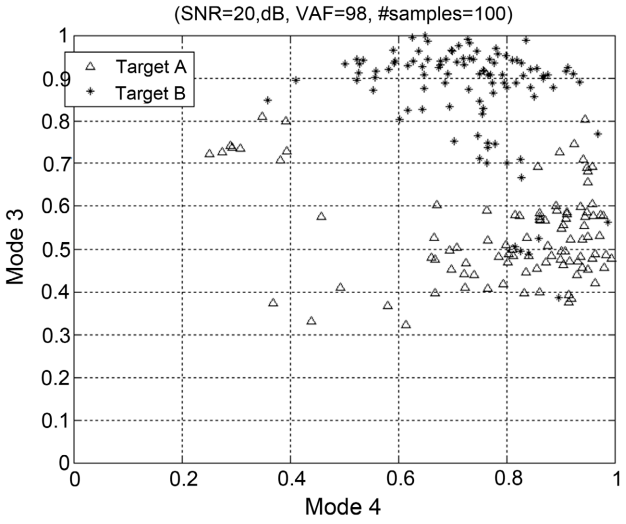

Figure 8. The feature space per third and fourth resonances for the perpendicular incidence direction.

In general, the depolarization degree appears most distinctive along the second to fourth resonances since these resonances excite the wing and tail sections of the target, respectively. This distinctiveness coincides with the degrees of the two targets differing along these sections.

The evaluation of the ROC performance undergoes a training process under *SNR* levels similar to that of the test sample. Figure 9 depicts the identification performances per resonance with only the modal order constraint $M = 4$ applied. Identification improves with more resonance in the feature set, e.g. the ROC of the combined third and fourth modes, compared to the individual ROC of the third or fourth modes.

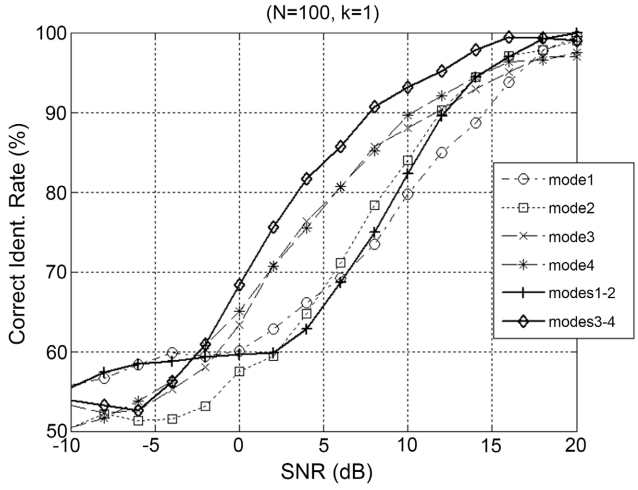

Figure 9. The identification performance per modes of interest.

Generally, the third and fourth have the best performance, reaching the lower bound of 50% near −10 dB.

5. Conclusion

The paper evaluated the ability of the depolarization degree to identify swept changes in a simple wire target that resembles an aircraft. Such a feature set is compact, reflects the target's dimensions and configuration attributes, is invariant to orientation, forms a recognizable pattern in the proposed feature space, and is resilient to ambiguity in the late time onset and noise compared to the symmetry and tilt degrees. Adding the constraints on the modal order M and VAF improved the certainty in the resonance set and thus the performance of the ROC; in this case, it achieved an identification rate with a lower bound below −10 dB and an upper bound of 100% at 20 dB. In future work, the identification approach must consider estimating the expected feature set with aspect variation. Therefore, the diversity of the target's look angle should be considered, and other decision-making algorithms, such as the nearest neighbor or statistical methods, should be exploited, especially nonparametric types and fuzzy logical approaches.

Conflicts of Interest

The author declares no conflicts of interest regarding the publication of this paper.

References

[1] Wu, J., Zhang, H. and Gao, X. (2021) Radar High-Resolution Range Profile Target Recognition by the Dual Parallel Sequence Network Model. *International Journal of Antennas and Propagation*, **2021**, Article ID: 4699373. https://doi.org/10.1155/2021/4699373

[2] Ma, Y., Zhu, L. and Li, Y. (2018) HRRP-Based Target Recognition with Deep Contractive Neural Network. *Journal of Electromagnetic Waves and Applications*, **33**, 911-928. https://doi.org/10.1080/09205071.2018.1540309

[3] Liu, J. and Wang, B.F. (2018) Dynamic Aircraft Identification Using HRRP under Attitude Perturbation Interference. *Journal of Electromagnetic Waves and Applications*, **33**, 929-945. https://doi.org/10.1080/09205071.2018.1555493

[4] Wang, C., Pei, J., Luo, S., Huo, W., Huang, Y., Zhang, Y., *et al.* (2023) SAR Ship Target Recognition via Multiscale Feature Attention and Adaptive-Weighed Classifier. *IEEE Geoscience and Remote Sensing Letters*, **20**, 1-5. https://doi.org/10.1109/lgrs.2023.3259971

[5] Li, X., Zhou, L., Wu, H., Yang, B., Zhang, W., Gu, J., *et al.* (2023) A Min-Pooling Detection Method for Ship Targets in Noisy SAR Images. *IEEE Access*, **11**, 31902-31911. https://doi.org/10.1109/access.2023.3262804

[6] Grathwohl, A., Meinecke, B., Widmann, M., Kanz, J. and Waldschmidt, C. (2023) UAV-Based Bistatic SAR-Imaging Using a Stationary Repeater. *IEEE Journal of Microwaves*, **3**, 625-634. https://doi.org/10.1109/jmw.2023.3253667

[7] Shi, F., Li, Z., Zhang, M. and Li, J. (2022) Analysis and Simulation of the Micro-Doppler Signature of a Ship with a Rotating Shipborne Radar at Different Observation Angles. *IEEE Geoscience and Remote Sensing Letters*, **19**, 1-5. https://doi.org/10.1109/lgrs.2022.3166209

[8] Morris, P.J.B. and Hari, K.V.S. (2021) Detection and Localization of Unmanned Aircraft Systems Using Millimeter-Wave Automotive Radar Sensors. *IEEE Sensors Letters*, **5**, 1-4. https://doi.org/10.1109/lsens.2021.3085087

[9] Garren, D.A., Odom, A.C., Osborn, M.K., Goldstein, J.S., Pillai, S.U. and Guerci, J.R. (2002) Full-Polarization Matched-Illumination for Target Detection and Identification. *IEEE Transactions on Aerospace and Electronic Systems*, **38**, 824-837. https://doi.org/10.1109/taes.2002.1039402

[10] Aldhubaib, F. and Shuley, N.V. (2010) Radar Target Recognition Based on Modified Characteristic Polarization States. *IEEE Transactions on Aerospace and Electronic Systems*, **46**, 1921-1933. https://doi.org/10.1109/taes.2010.5595604

[11] Baum, C. (2006). Combining Polarimetry with SEM in Radar Backscattering for Target Identification. 2006 3*rd International Conference on Ultrawideband and Ultrashort Impulse Signals*, Sevastopol, 18-22 September 2006, 11-14. https://doi.org/10.1109/uwbus.2006.307150

[12] Aldhubaib, F. (2020) Generic Aircraft Model Recognition by Two Shape Factors: In the Resonance Region. *IET Radar, Sonar & Navigation*, **14**, 81-88. https://doi.org/10.1049/iet-rsn.2019.0089

[13] Aldhubaib, F.F.H. (2020) Enhancing the SEM Signature via the Optimum Onset with a Bistatic and Cross-Polarization Radar Configuration. *IEEE Access*, **8**, 86238-86245.

https://doi.org/10.1109/access.2020.2992459

[14] Aldhubaib, F. (2022) Composite Gaussian Pulsed Waveform for Robust Resonance Radar Signal. *The Journal of Engineering*, **2023**, e12216. https://doi.org/10.1049/tje2.12216

[15] Aldhubaib, F. (2022) Enhancing SEM Signature via Bistatic Radar Configuration of Small Bisectors. *IET Radar, Sonar & Navigation*, **16**, 1053-1064. https://doi.org/10.1049/rsn2.12242

[16] Alhajri, A. and Aldhubaib, F. (2023) Waveform Design for Resonance Signature of Fighter-Class Target. *IET Radar, Sonar & Navigation*, **17**, 1812-1821. https://doi.org/10.1049/rsn2.12466

[17] Yan, H., Li, J. and Liao, G. (2007) Multitarget Identification and Localization Using Bistatic MIMO Radar Systems. *EURASIP Journal on Advances in Signal Processing*, **2008**, Article No. 283483. https://doi.org/10.1155/2008/283483

[18] Rihaczek, A.W. and Hershkowitz, S.J. (2000) Theory and Practice of Radar Target Identification. Artech House.

[19] Duda, R.O., Hart, P.E. and Stork, D.G. (2001) Pattern Classification. 2nd Edition, Wiley.

[20] Jain, A.K., Duin, P.W. and Jianchang Mao, (2000) Statistical Pattern Recognition: A Review. *IEEE Transactions on Pattern Analysis and Machine Intelligence*, **22**, 4-37. https://doi.org/10.1109/34.824819

[21] Sarkar, T.K. and Pereira, O. (1995) Using the Matrix Pencil Method to Estimate the Parameters of a Sum of Complex Exponentials. *IEEE Antennas and Propagation Magazine*, **37**, 48-55. https://doi.org/10.1109/74.370583

[22] Aldhubaib, F. (2016) Stability of Target Resonance Modes: In Quadrature Polarization Context. I*nternational Journal of Engineering Research and Applications*, **6**, 39-42.

[23] Feko Suite 7.0. (2014) Altair, South Africa. https://altair.com/feko/